Lateral pressures on underground stiff box structures from sinusoidal motions

Craig A. Davis, Ph.D.
Los Angeles Department of Water and Power, Los Angeles, CA, USA
Shideh Dashti, Ph.D.
Department of Civil, Environmental, & Arch. Engineering, University of Colorado Boulder, USA
Ashkaan Hushmand, Ph.D.
Hushmand Associates Inc., Irvine, CA, USA

ABSTRACT
Lateral seismic earth pressures on shallow stiff underground structures are evaluated and compared between analytical and physical models. An analytical model is presented for evaluating the dynamic increment of lateral earth pressures on perfectly rigid, unyielding walls subject to vertically propagating shear waves. In this paper, we compare the analytical model predictions to physical model measurements obtained from centrifuge testing. Centrifuge experiments evaluated the seismic response of a stiff underground box structure for base sinusoidal motions of amplitude near 0.3g and primary frequencies of 0.33, 1, 2, 3, 4, 5, and 6 Hz, in addition to other broadband earthquake motions. The response of the stiff structure used in the physical models approximates the rigid structure assumptions of the analytical model. Model comparisons are made for the dynamic increment of lateral earth pressures. Results show the analytical model based on the most dominate modes contributing to lateral seismic pressures compares well with the experimental measurements for the conditions and type of underground structure considered in this study. The evaluation shows maximum seismic lateral stresses on stiff underground structures can be accurately estimated assuming rigid walls and using the mean contributing frequency f_{mc} with a mode having equivalent wavelength of four times the structure depth H.

1 INTRODUCTION

The seismic response of underground structures is a complex soil-structure interaction problem dependent upon the properties of earthquake motion, surrounding soil, and structure. There are many different analytical and numerical models attempting to capture the complex dynamic soil and structure kinematic interactions. However, there are few good-quality tests for which to validate the existing models. Centrifuge tests were undertaken at the University of Colorado Boulder to improve our understanding of the physics underlying the seismic behavior of buried structures. The results of these tests are used to make an initial comparison of an analytical model which evaluates underground rigid structures in a viscoelastic soil medium subjected to vertically propagating seismic waves. This paper first describes the analytical model, then the centrifuge experiments, followed by an initial comparison in terms of seismic lateral earth pressures using sinusoidal motions with primary frequencies of 0.33, 1, 2, 3, 4, 5, and 6 Hz.

2 ANALYTICAL MODEL

Figure 1 shows a model introduced by Davis (2003) used to develop a simplified analytical method to calculate dynamic earth pressures from propagating waves on the walls of a perfectly rigid-unyielding underground structure embedded in an infinite elastic half-space. This model compared well to Wood (1973) and Veletsos and Younan (1994) (Davis 2003).

Figure 1a shows the model for evaluating lateral stresses on underground rigid box structures embedded within an infinite half-space. The half-space represents a deep unsaturated inhomogeneous viscoelastic soil deposit having a unit weight γ, shear modulus G, hysteretic damping ratio ξ, and Poisson ratio ν. γ, ξ, and ν are considered constant, while G varies with depth. The structure has a width W, vertical rigid walls of height h, and is buried a depth d with its base at depth H below the stress-free ground surface. The structure is assumed to have an infinite length L satisfying plain strain conditions. The model is defined by the x-z and x_1-z_1 coordinate systems originating at the ground surface and top of wall, respectively, which are related by $x = x_1$ and $z = z_1 + d$.

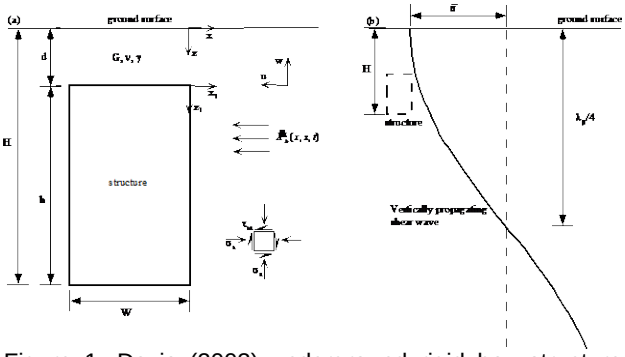

Figure 1. Davis (2003) underground rigid box structure model: a) structure geometry and coordinate systems, and b) wave propagation model at ground surface

The structure is subjected to vertically incident shear waves. The horizontal and vertical motion in the soil medium is represented by displacements u and w, respectively, having positive motions as defined in Figure 1a. Figure 1a also shows the stress sign convention

where compressive stresses are defined as positive. The dynamic increment of earthquake pressure σ_x is given by:

$$\sigma_x = k_s u = k_s(u_f - u_H) \qquad d \le z \le H \qquad [1]$$

Davis (2003) also proposed a lateral stress increase with soil densification $\Delta\sigma_h$, which will not be addressed in this paper. In Equation 1, k_s is a continuous soil stiffness parameter, u is the horizontal displacement function, u_f is the horizontal free-field soil deformation during seismic shaking, u_H is the horizontal free-field soil deformation at depth H. The closed form analytical solution using elastic wave propagation theory is presented in Davis (2003), and only some of the results will be summarized herein. The horizontal displacement is given by:

$$u = \bar{u}\left(1 - e^{-k_\beta x_1/\psi_e}\right)\left(\cos k_\beta(z_1 + d) - \cos k_\beta H\right),$$
$$\psi_e^2 = \frac{2-\nu}{1-\nu},\ H \le \lambda_\beta/4 \qquad [2]$$

where $\bar{u}$ is the horizontal free-field displacement at the ground surface, λ_β is the shear wavelength, $k_\beta = \omega/\beta$ is the shear wave number, $\omega = 2\pi f$ is the angular frequency, f is the wave frequency, β is the free-field shear wave velocity of the soil. The harmonic nature of the motion described by $e^{-i\omega t}$ is implied in Equation 2 and subsequent functions.

The Davis (2003) model assumed the soil stiffness varied with depth, but G in the wall vicinity and in the free-field were modified similarly based on the shear strain experienced in the free-field (i.e. G was constant for all x at any depth z). In addition, for practical application, the shear wave velocity was assumed a constant average value over wall height. However, the free-field and near-wall strains are not equal and β may vary with depth along with G. Thus the model presented herein investigates the soil stiffness variation using the shear modulus G_{xz}, which is not a constant value but varies primarily as a function of void ratio, relative density, plasticity index, mean effective stress, shear strain, and number of shearing cycles (Hardin and Drnevich, 1972; Ishibashi and Zhang, 1993).

In the free-field, the initial small strain shear moduli, $G_i^* = G_i\ /(1 + 2i\xi)$, in the absence of seismic shaking is determined at any depth z from:

$$G_i^* = G_0(1 + 2i\xi) f_G(z);\ f_G(z) = (z/H)^m \qquad [3]$$

where $G_0 = G_0^*/(1 + 2i\xi)$ is the reference free-field small strain modulus at depth H, and $f_G(z)$ is a function representing the variation in shear moduli with depth. The inhomogeneity coefficient m varies as a function of plasticity index and shear strain amplitude; the value of m typically ranges from ½ for small strains to 1 at large strains (Hardin and Drenovich, 1972). When a seismic shear strain is applied the shear modulus varies as:

$$G_{xz} = \Omega_{xz} G_0 f_G(z) \qquad [4]$$

Ω_{xz} is a coefficient defining how G_{xz}/G_0 varies with shear strain (e.g., Ishibashi and Zhang, 1993) at a specified depth. The shear strain function presented in Equation 8 below varies with x_1 and z and becomes that of the free-field (i.e., independent of x_1) at approximately $x_1 = 3h$, where $\Omega_{xz} = \Omega_{fz}$. Thus, Ω_{xz} is a continuous function varying from Ω_{sz} at $x_1 = 0$ to Ω_{fz} at $x_1 = 3h$ for a given depth. Using this notation, the shear modulus can be defined at any x and z coordinate, where the subscripts s and f indicate the shear modulus at the structure or in the free-field, respectively, and the subscript H indicates the reference modulus at depth $z = H$.

The soil stiffness parameter is:

$$k_s = G_{xz}\frac{\omega}{\beta}\psi_\sigma e^{\omega x_1/\beta\psi_e},\ \psi_\sigma = \frac{2}{\sqrt{(1-\nu)(2-\nu)}} \qquad [5]$$

The shear wave velocity of the soil medium is:

$$\beta = \sqrt{gG_{fH}/\gamma}\left(\frac{z}{H}\right)^{\frac{m}{2}} = \sqrt{g\Omega_{fH}G_0/\gamma}\left(\frac{z}{H}\right)^{\frac{m}{2}} \qquad [6]$$

where g is the acceleration of gravity. β_0 is the small strain shear wave velocity associated with $G_{fH} = G_0$ (i.e., $\Omega_{fH} = 1$). At depth H the reference shear wave velocity is $\beta = \sqrt{gG_{fH}/\gamma}$. The free-field displacement u_f for $H \ge z \ge 0$ defined by Davis (2003) as $x_1 \ge 3h$ is given by:

$$u_f = \bar{u}\left(\cos 2\pi\frac{z_1 + d}{\lambda_\beta} - \cos\frac{2\pi H}{\lambda_\beta}\right) \qquad [7]$$

The shear strain ε_{xz} and shear stress τ_{xz} are given by:

$$\varepsilon_{xz} = \bar{u}k_\beta^2\left\{\left(1 - \frac{2}{\psi_e^2}e^{-k_\beta x_1/\psi_e}\right)\frac{1}{k_\beta}\sin k_\beta(z_1 + d) - \frac{\nu}{2-\nu}e^{-k_\beta x_1/\psi_e} z\cos k_\beta H\right\} \qquad [8]$$

and $\tau_{xz} = G_{xz}\varepsilon_{xz}$

Substituting Equations 3 to 7 into Equation 1 at $x_1 = 0$ gives:

$$\sigma_x = \frac{\bar{u}\gamma}{g}C_G\psi_\sigma\beta_0\omega\left(\frac{z_1 + d}{H}\right)^{C_m}\left[\cos\left(\frac{2\pi f}{\beta}(z_1 + d)\right) - \cos\left(\frac{2\pi f}{\beta}H\right)\right] \qquad [9]$$

where σ_x is the compressive stress against the structure. C_G and C_m are functions of Ω_{xH} and m, respectively, explained at the end of this section. Equation 9 shows the lateral stresses applied to the structure depend upon the frequency of input motion because of the soil stiffness parameter in Equation 5. The stress amplitude in Equation 9 is independent of frequency when the velocity amplitude $\bar{v} = -\bar{u}\omega$ is substituted for $\bar{u}$.

Motions are usually made up of multiple waves of different frequency f_p, where p is the number of wave frequencies making up the motions striking at the same

time. For these compound motions the stress on the wall is a result of the displacement superposition from each wave of frequency f_p. Equations 2, 5, and 7 (substituting $|\bar{v}|$), respectively, become:

$$u = \bar{u}\sum_p \frac{a_p}{\sum_p a_p}\left(1 - e^{-k_{\beta p}x_1/\psi_e}\right)\left(\cos k_{\beta p}(z_1+d) - \cos k_{\beta p}H\right) \quad [10]$$

$$k_{sp} = G_{xz}\frac{\omega_p}{\beta}\psi_\sigma e^{\omega_p x_1/\beta\psi_e} \quad [11]$$

$$\sigma_x = \frac{\bar{v}\gamma}{g}C_G\psi_\sigma\beta_0\left(\frac{z_1+d}{H}\right)^{C_m}S\,,$$

$$S = \sum_p \frac{a_p}{\sum_p a_p}\left[\cos\left(\frac{2\pi f_p}{\beta}(z_1+d)\right) - \cos\left(\frac{2\pi f_p}{\beta}H\right)\right] = \frac{u(z)}{\bar{u}} \quad [12]$$

Where a_p is the Fourier coefficient for wave p of frequency f_p. The shape function S is derived from the Equation 12 free field motion and assumes all waves of frequency f_p reflect off the surface at the same time and direction (i.e., Equation 12 does not account for phase difference in waves along the wall height).

The form of functions C_G and C_m are difficult to identify based primarily on G and m being nonlinear functions of x_1 and z. Additionally, the assumption of Equation 1 requires the shear modulus in the exponential term in Equation 2 to be that of the free field, whereas it also represents a parameter changing with x_1. As a result, estimating k_s at the wall ($x_1 = 0$) based on ε_{xz} is not only difficult, but also is expected to overestimate soil stiffness; Equation 8 indicates ε_{xz} is smallest at $x_1 = 0$ resulting in largest modulus G_{sz}. Incorporating the influence of shear strain on shear modulus, k_s should represent an effective stiffness applied at $x_1 = 0$, defined by C_G and C_m, but determined as an average over some horizontal distance between the structure and free field and defined by the following:

$$k_{sp} = G_0 C_G \frac{\omega_p}{\beta}\psi_\sigma\left(\frac{z}{H}\right)^{C_m} \quad [13]$$

Values for C_G and C_m are identified in this paper using results of physical modeling.

3 PHYSICAL MODEL

Dynamic tests of model buried reservoirs were performed at 60g centrifugal acceleration using the 5.5 m-radius, 400 g-ton geotechnical centrifuge at the University of Colorado Boulder. The model specimens were prepared in a flexible shear beam (FSB) container (Ghayoomi et al. 2013).

The response of the system during testing was measured using 27 accelerometers, 8 LVDTs, 16 strain gauges (8 on each wall), 4 tactile pressure transducers (2 on each wall), and 16 earth pressure cells (8 on each wall). The location of the transducers is shown in Figure 2. Each tactile sensor (manufactured by Tekscan Inc.) contained 14 rows and 14 columns of sensels (sensing points) amounting to 196 sensels, each 5.1 mm by 5.1 mm. Each of the 196 sensels recorded pressure data at a rate of 4,000 samples/sec during the dynamic centrifuge tests. All recordings were synchronized except for the tactile sensors that had a separate data acquisition system.

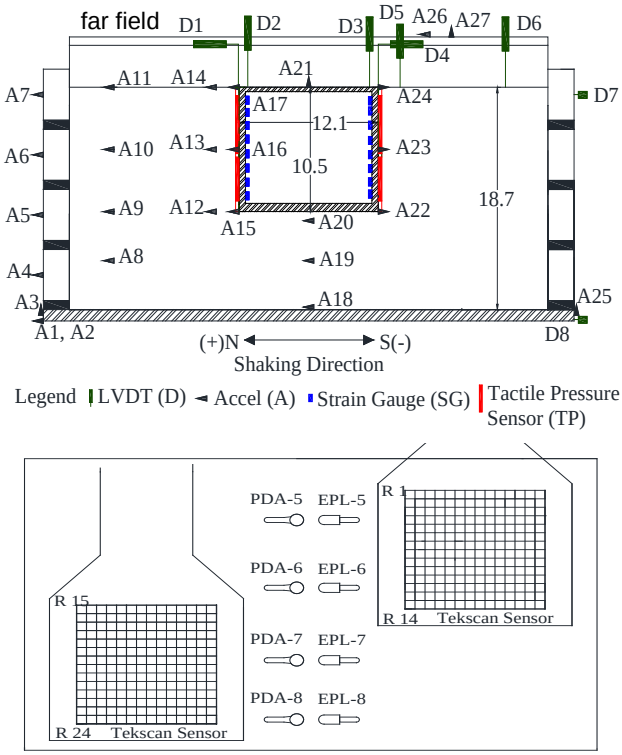

Figure 2. Top: Instrumentation layout of a representative centrifuge test (dimensions shown in prototype scale meters). Bottom: Pressure sensor layout on each wall of the buried structure.

A free-field test was also performed using 16 accelerometers and 7 LVDTs as shown in Figure 3. Dry Nevada sand No. 120 (G_s=2.65; e_{min}=0.56; e_{max}=0.84; D_{50}=0.13 mm; C_u=1.67) was pluviated in the FSB container at a target relative density of D_r=60% (γ_d=15.6 kN/m^3). The soil deposit was dry pluviated in layers using a hopper at a calibrated height to achieve the target D_r. The total soil depth was D = 18.7 m in prototype scale.

Scaled model structures with different stiffness values were designed based on a simplified version of prototype buried reservoir structures by maintaining similar natural frequencies and lateral stiffness (detailed by Hushmand et al. 2016a,b,c). All model structures were constructed of four pieces of welded 1018 Carbon Steel (density = 7870 kg/m^3; Young's modulus = 2×10^8 kPa). The dimensions of the stiffer structure modeled experimentally were: outer height = 10.4 m, outer width = 12.1 m, base thickness = 1.46 m, roof thickness = 1.12 m, and wall thickness of 1.13 m. The fundamental frequency of the stiff structure was experimentally and numerically calculated at 9 to 10 Hz.

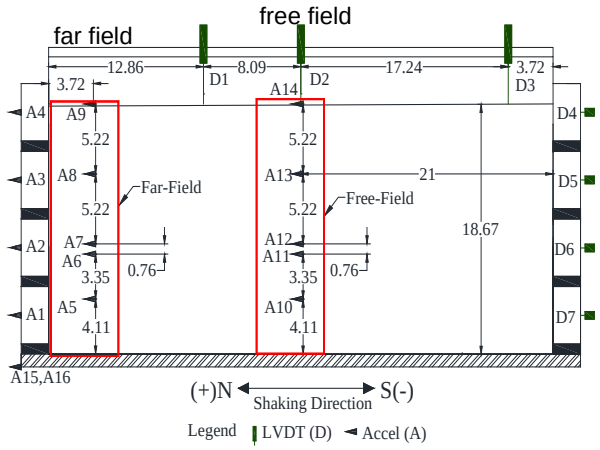

Figure 3. Instrumentation layout for free-field test (dimensions shown in prototype scale meters).

Ground motions were applied to the base of model specimens in flight using the servo-controlled, electro-hydraulic shake table (Ketcham et al. 1991) mounted on the basket at the end of the centrifuge arm. A series of seven horizontal earthquake motions and seven sinusoidal motions (15 cycles) were applied to the base of the model specimen in the order listed in Table 1. The amplitude of sinusoidal motions was kept about the same, while their frequencies were varied. The achieved sinusoidal input motions were dominated by the frequencies for which they were identified, but they also contained other frequencies of importance.

The test procedures and results are provided in Hushmand (2016) and HAI (2016). The physical and analytical models are compared in this paper using the sinusoidal motions and pressures on the north and south walls, assuming the stiff structure used in the centrifuge experiments approximated a perfectly rigid structure.

Table 1. Base motion characteristics as achieved in centrifuge (prototype scale)

	Input motion parameters			
Shake Event	PGA (g)	I_a (m/s)	$D_{5\text{-}95}$ (s)	f_m (Hz)
Northridge-L	0.30	1.42	21.14	1.2
Northridge-M	0.78	5.5	27.6	1.47
Northridge-H	1.15	11.86	27.23	1.64
Izmit-1	0.32	2.75	38.8	---
Sine 0.33 Hz	0.29	---	15	---
Sine 1 Hz	0.32	---	15	---
Sine 2 Hz	0.34	---	15	---
Sine 3 Hz	0.42	---	15	---
Sine 4 Hz	0.39	---	15	---
Sine 5 Hz	0.51	---	15	---
Sine 6 Hz	0.46	---	15	---
Northridge-L-2	0.30	1.73	18.5	1.28
Izmit-2	0.33	2.78	38	1.75
Loma	1.14	14.27	12.77	2.38

4 EXPERIMENTAL RESULTS

The sine wave acceleration time histories for 0.33, 1, 2, 3, 4, 5, and 6 Hz motions were integrated to obtain velocity and displacement. These were baseline corrected with a cubic polynomial and filtered using a 6th order Butterworth bandpass between 0.3 and 25 Hz. The displacement time histories required an additional linear baseline correction. The Sine 1 Hz shake event surface far-field motion and Fourier amplitude spectrum at A11 are shown in Figure 4.

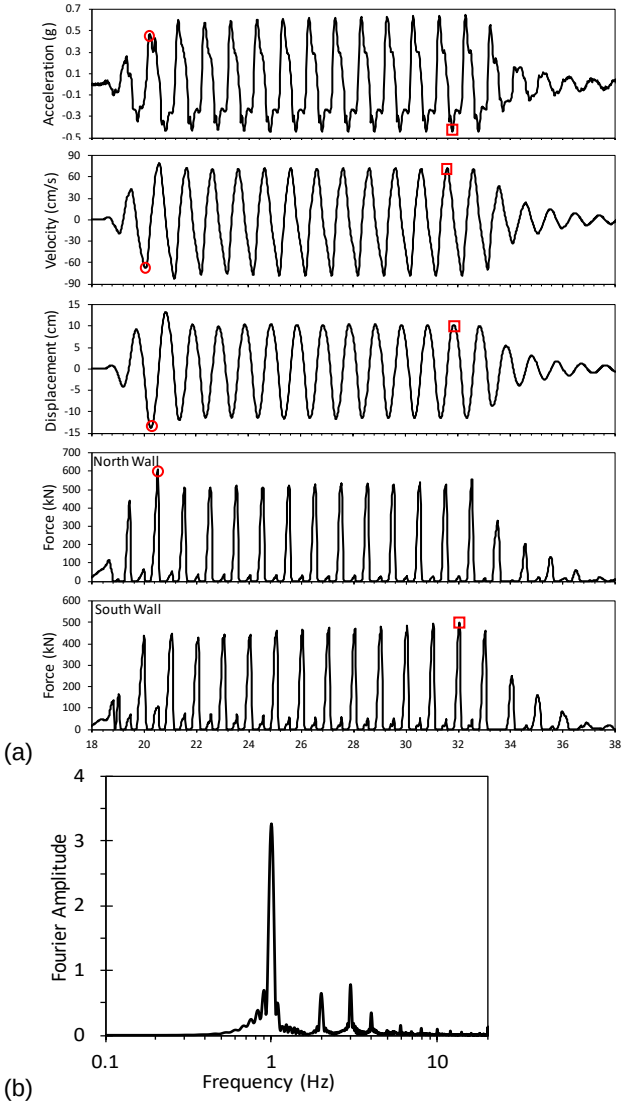

Figure 4. (a) Sine 1 Hz shake event acceleration, velocity, displacement time histories recorded at A11, and resultant force (compression is positive). Circles and squares represent values at time used for comparing models on north and south walls, respectively. (b) Fourier spectra for records in (a).

Sites having shear modulus varying with depth per Equation 3 do not necessarily have one distinct natural frequency. Modal frequencies were evaluated from the transfer function of surface to base accelerations in the far-field using pre-shaking recorded ambient vibrations. These frequencies were used to estimate the small strain shear wave velocity and shear modulus which was then compared to that obtained using Seed and Idriss (1970) and variation with depth for m = 0.5. The site modal frequencies of about 6 and 7.4 Hz, were identified to

correspond with $\beta_i = 4f_0H_{site}$ = 525 m/s at container base and β_0 = 450 m/s.

The tactile sensor pressure recordings were aligned in time by matching records with the PDA and EPL recordings. Unfortunately, there were only a few good PDA and EPL recordings, and therefore these will not be presented. The dynamic increment of pressure was estimated from the tactile sensors as the difference between the total and pre-shake, static lateral earth pressure for each of the recordings. The recorded data was pre-processed to reduce scatter as described by Hushmand et al. (2016b). The pressure was numerically integrated to obtain force as shown in Figure 4.

5 LATERAL EARTH PRESSURE EVALUATION

Lateral pressures are evaluated at time of largest dynamic force. Negative soil displacements apply increased pressure to the north wall while positive soil displacements apply increased pressure on the south wall. Table 2 presents the ground motion parameters associated with each peak force. Two motions are used here to evaluate the lateral pressures and compare with the analytical model: The Sine 1 Hz and Sine 0.33 Hz shake events.

Table 2. Motion parameters at the time of maximum dynamic force (Frc = Force).

Shake Event	Wall	Acc (g)	Vel (m/s)	Dis (m)	Frc (kN)
Sine 0.33 Hz	N	-0.16	0.52	0.22	271
	S	0.22	-0.56	-0.20	317
Sine 1 Hz	N	0.47	-0.68	-0.14	610
	S	-0.44	0.72	0.10	499
Sine 2 Hz	N	0.56	-0.25	-.017	264
	S	-0.26	0.22	0.013	311
Sine 3 Hz	N	0.43	-0.19	-0.012	318
	S	-0.79	0.26	0.0098	330
Sine 4 Hz	N	0.45	-0.12	-0.0042	209
	S	-0.73	0.19	0.007	283
Sine 5 Hz	N	0.36	-0.091	-0.0012	204
	S	---	---	---	---
Sine 6 Hz	N	0.51	-0.15	-0.010	163
	S	-0.37	0.10	0.0099	190

Parameters in the analysis include d = 0, ν = 0.3, γ = 15.9 kPa. The value of γ is based on the initial unit weight described by Hushmand et al. (2016a) and the increase in value from settlement presented in Hushmand et al (2016b). The damping ratio is not needed for the calculation since the wave solution is based on measured surface motions.

Average strains were calculated between each adjacent set of far-field recordings between A2 and A11 (see Fig. 2). From these strains Ω_{fH} was calculated using (Ishibashi and Zhang, 1993), and the resulting β, which are presented in Table 3.

5.1 Shape Function Evaluation

The measured site response values from the free-field (Fig. 3) and buried structure (Fig. 2) tests were used to estimate an apparent shear wave velocity β_{app}, which is associated with an apparent frequency and wavelength. Figure 5 diagrams the apparent wavelength λ_{app}. Table 3 presents β_{app}. As seen in Figure 5, when multiple waves superimpose, the peak values result in λ_{app}, differing from source wavelengths. λ_{app} results from the superposition of waves having different frequency and phase. The resulting ground displacement amplitude and curvature are important parameters causing pressure on the walls.

Table 3. Estimated β, β_{app}, f_{mc}, and $\beta'_{app.}$

Shake Event	Wall	β (m/s)	β_{app} (m/s)	f_{mc} (Hz)	β'_{app} (m/s)
Sine 0.33 Hz	N	393	230	5.2	217
	S	401	230	5.2	217
Sine 1 Hz	N	150	150	3.5	146
	S	132	132	3.5	146
Sine 2 Hz	N	394	270	6.0	250
	S	403	230	6.0	250
Sine 3 Hz	N	391	230	6.0	250
	S	392	260	6.0	250
Sine 4 Hz	N	411	190	8.0	334
	S	416	230	8.0	334
Sine 5 Hz	N	429	210	7.5	313
	S	---	---	---	313
Sine 6 Hz	N	406	406	9.7	404
	S	418	418	9.7	404

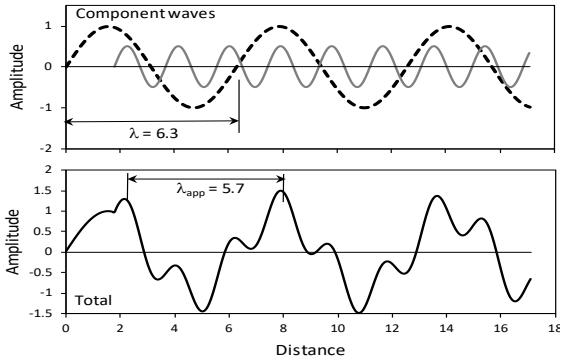

Figure 5. Diagram explaining apparent wavelength.

As previously explained, the analytical model does not account for the phase difference in propagating waves. The phase difference is estimated by fitting the site response and shape functions to match recorded values.

Figure 6 shows the estimated Sine 1 Hz shake event site response and shape function in the far-field measured at A8 to A11 at the time of north wall maximum force. Also shown for comparison are displacement ratios from the free-field model shown in Figure 3 measured at A14 to A15. The free-field model is presented for comparison, at the equivalent cycle number, because in a small container test with a model buried structure, far-field motions are not completely representative of free-field motions since they are not measured a distance of 3h from the structure. The estimated response used Fourier coefficients shown in Fig. 4b for frequencies 1 to 8 Hz. The far-field β_{app} = 150 m/s in Table 4 was identified by fitting the curve in Figure 6 to best match the measured values. β_{app} was applied as a constant over the entire depth. As indicated in Figure 6, in the buried structure test, the far-field motions are comparable to the free-field test motions (without any structure). As indicated in Table 4, β_{app} equals β for the Sine 1 Hz and Sine 6 Hz shake events, but not for any other events.

Except for the Sine 0.33 Hz, for each shake event β_{app} was estimated by fitting the measured site response and shape function similar to that shown in Figure 6. The process for evaluating the Sine 0.33 Hz shake event is described later. The Fourier coefficients used for each shake event was capped at 8 Hz except for the Sine 3 Hz, 5 Hz, and 6 Hz shake events which, respectively, were capped at frequencies 9 Hz, 10, Hz, and 12 Hz.

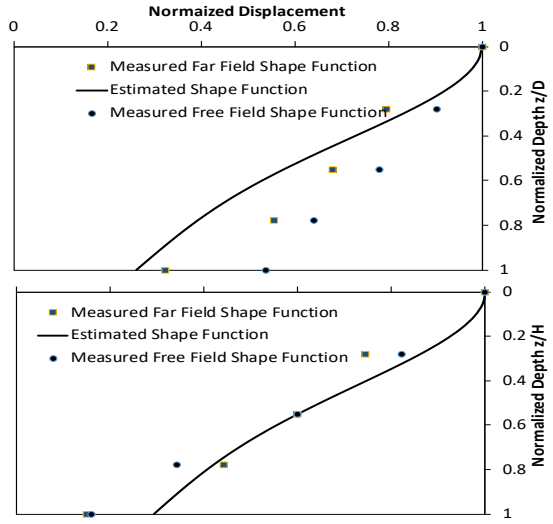

Figure 6. Sine 1 Hz shake event site response (top) and shape function (bottom) at the time of maximum dynamic force on the north wall. Shape function is presented for the entire container depth to show trends.

Figure 7 shows the contributions to *S* for the Sine 1 Hz shake event. As indicated, the 1 Hz frequency is not the greatest contributor to the earth pressures, even though this motion is the greatest component of site response in the far-field. As indicated in Figure 7, the greatest contributors to lateral earth pressures for the Sine 1 Hz shake event are the 3 Hz and 4 Hz wave modes, followed by the 1 Hz and 6 Hz modes. Even though the 1 Hz mode has the largest amplitude, its wavelength is much larger and the relative displacement has a lesser effect than the shorter length and lower amplitude 3 Hz and 4 Hz modes.

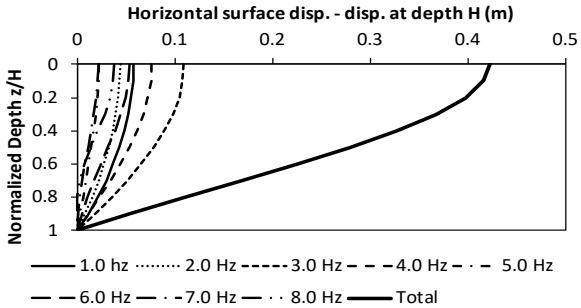

Figure 7. Modal contributions, Sine 1 Hz shake event.

Figure 8 presents maximum pressure distribution with the estimated σ_x using Equation 12 for C_G = 1.0 and C_m = 1.0. The Sine 5 Hz shake event did not record pressures on the south wall. As seen in Figure 8, Equation 12 is useful for estimating the maximum pressure during all motions for C_G = 1.0 and C_m = 1.0 when the shape function can be estimated using analytical methods. The estimated pressures match extremely close or exceed the measured values for all cases except the Sine 6 Hz shake event on the south wall. The estimated lateral pressures for the Sine 1 Hz and Sine 2 Hz shake events compare very closely with the measured values.

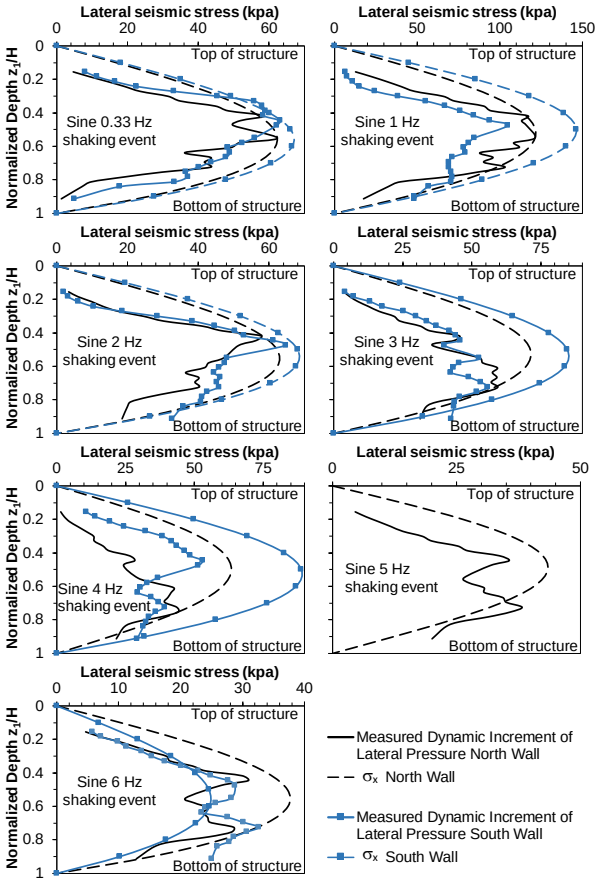

Figure 8. Comparison of σ_x with measured pressure distribution for north and south walls from all sinusoidal shake events.

5.2 Sine 0.33 Hz Shake Event Response

Discrepancies in response for the Sine 0.33 Hz shake event were identified when applying the shape function evaluation method for estimating pressures. For all other events, β_{app} was essentially the same value when comparing site response and the shape function. However, as shown in Figure 9, this is not true for the Sine 0.33 Hz shake event. The β_{app} value in Table 3 is that most closely fitting the shape function while β most closely fits the site response. Further, the peak pressures, as shown in Figure 10, on the north wall for the Sine 0.33 Hz shake event occur on positive displacements (when soil is moving away from the wall) and negative peak displacement on the south wall. Whereas the opposite is true for all other shake events (see Figure 4) and for the analytical model.

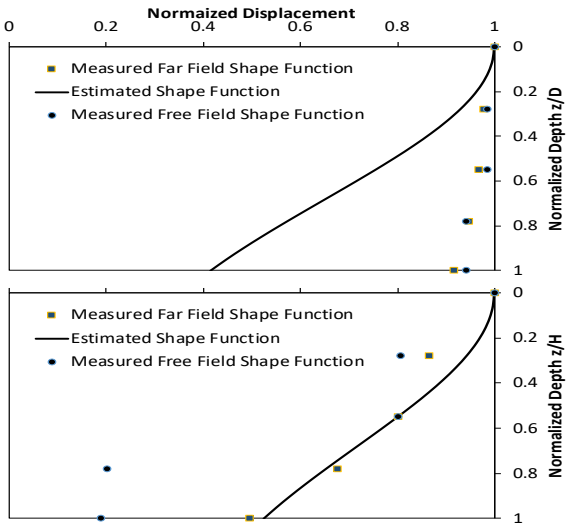

Figure 9. Sine 0.33 Hz shake event site response (top) and shape function (bottom) at time of maximum dynamic force on north wall. Shape function presented for entire container depth to show trend.

Figure 11 shows the modes contributing to lateral pressure on the walls. As seen in Figure 11, there are many contributing modes. Figure 11 identifies the lowest frequencies (e.g., 0.33 and 0.66 Hz) provide no significant contribution to the total pressures on the wall because they have no effect on the shape function. The greatest contribution to the shape function comes from the higher frequencies ranging from 4.0 to 6.6 Hz. However, the lower frequency modes have the largest amplitudes. As a result, the Sine 0.33 Hz shake event propagated low frequency-large amplitude waves along with superimposed higher frequency-lower amplitude waves.

The variation in waves are identifiable in the acceleration time history, but not in the displacement or velocity time histories due to the integration process. The acceleration time history is dominated by the low frequency, large amplitude motion, but there clearly are very high frequency acceleration spikes. Close review of Figure 10 reveals the peak force on the south wall aligns with the positive high frequency acceleration spikes. Further review of the acceleration time history identifies the high frequency motion is about 180 degrees out of phase with the low frequency motion. This means as the low frequency motion is accelerating toward the wall, and displacing away from the wall, the high frequency motion is accelerating away from, and displacing toward the wall.

It is the superposition of low and high frequency waves and their phase variation which explain the difference in response between the Sine 0.33 Hz and the other shake events. The low period motions dominate the site response for the Sine 0.33 Hz shake event, but these motions provide essentially no contribution to the shape function. This differs from the other motions, which are exemplified in Figure 6 where the same modes dominate both site response and the shape function. Further, the high frequency motions displace into the wall, while the low frequency motions displace away from the wall. It is this low frequency displacement amplifying the wall pressures. Since they are superimposed on the low frequency-high amplitude waves, the time histories give the appearance of the pressure-inducing modes being anti-correlated for the Sine 0.33 Hz motion, compared with all other events, whereas in reality they are completely correlated.

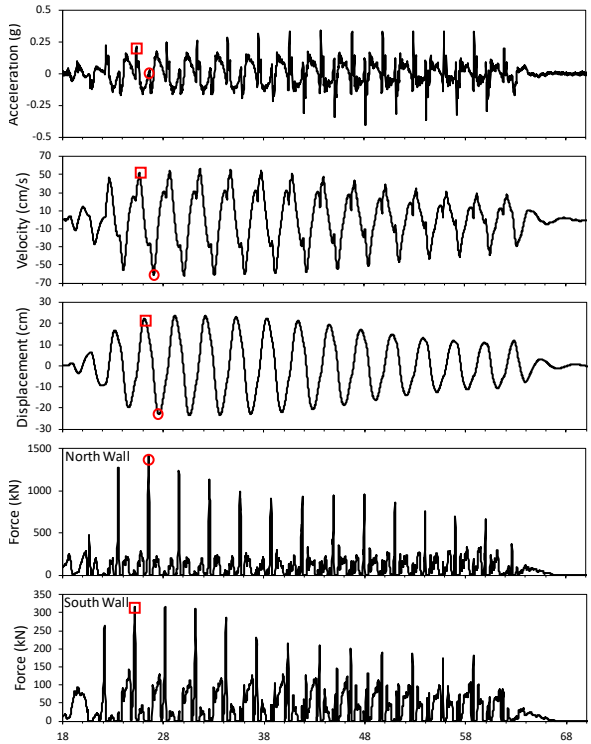

Figure 10. Sine 0.33 Hz shake event acceleration, velocity, displacement, and resultant force (compression is positive) time histories recorded at A11. Circles and squares represent values at time used for comparing models on north and south walls, respectively.

5.1 Evaluation of the Contributing Modes

The effect of most dominant modes is evaluated by identifying the mean contributing frequency, f_{mc}. f_{mc} is defined as the mean frequency from only those most dominant modes. The most dominant modes are defined as those which sum to be equal or greater than half the total shape function at ground surface. Using Figure 11 as an example, f_{mc} = (4.0+4.3+4.5+5.0+5.3+5.5+6.0+6.6)/8 = 5.2 Hz. In Figure 7 for example, f_{mc} = (1.0+3.0+4.0+6.0)/4 = 3.5 Hz. The sum of amplitudes at ground surface for each of these modes exceeds half the total shown in the respective figures. Table 3 summarizes f_{mc} for each shake event. f_{mc} can be considered an equivalent single frequency approximating the sum of total modes applying the wall pressure. The maximum pressure is applied for modes having a wavelength of 4H. From this, an apparent shear wave velocity can be estimated from $\beta'_{app} = 4Hf_{mc}$. These values are presented for each shake event in Table 3 and are found to be comparable to β_{app} within an accuracy of test measurement and data processing. This implies f_{mc} is equivalent to the apparent frequency described for the shape function evaluation.

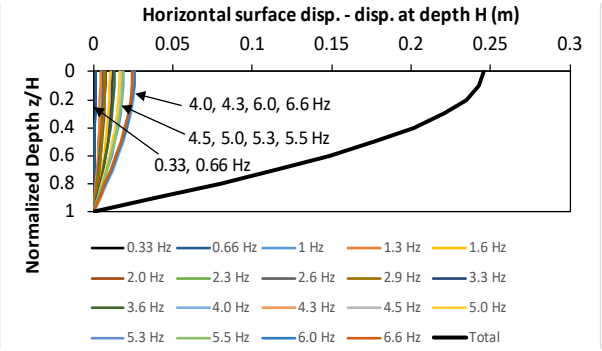

Figure 11. Modal contributions, Sine 0.33 Hz shake event.

Applying the β'_{app} values presented in Table 3 will produce effectively the same pressure calculations for each shake event except for the Sine 4 Hz and 5 Hz events. For these two events, the pressures would be calculated to be somewhat lower and higher, respectively, but would not change the conclusions presented herein.

6 CONCLUSIONS

The proposed analytical model developed for rigid buried structures compares very well with the centrifuge measured maximum dynamic increment of earth pressure for the range of input shaking and C_G = 1 and C_m =1. This indicates the most important parameters describing the basic physics of the underground soil-structure interaction problem as tested are incorporated into the analytical model. The contributing modes evaluation method using f_{mc} appears to be the most practical method of evaluation to cover the entire spectra of possible modes contributing to site and lateral pressure response. Evaluating seismic lateral earth pressures using measured shape functions produced similar results, but in practice for a forward analysis of a scenario earthquake, there is little guidance for estimating the shape function. As a result, lateral stresses on rigid underground structures can be accurately estimated using the mean contributing frequency f_{mc} with a mode having equivalent wavelength of four times the structure depth, which is expressed using an apparent shear wave velocity $\beta_{app} = 4Hf_{mc}$. The analytical pressure estimates matched the centrifuge recorded maximum pressures well when using a constant β_{app} over wall depth.

7 ACKNOWLEDGEMENT

The authors acknowledge support from the Los Angeles Department of Water and Power for centrifuge testing.

8 REFERENCES

Davis, C. A., 2003, “Lateral Seismic Pressures for Design of Rigid Underground Structures, *Proc. 6th U.S. Conf. on Lifeline* Eq. *Engineering, Monograph 25,* ASCE, Long Beach, Aug., 10-13, pp. 1001-1010.

Ghayoomi, M., Dashti, S., & McCartney, J. S. (2013). “Performance of a transparent Flexible Shear Beam container for geotechnical centrifuge modeling of dynamic problems”. *Soil Dynamics and Eqk. Engineering*, *53*, 230-239

Hardin, B. O., and V. P. Drnevich, 1972, “Shear Modulus and Damping in Soils: Measurements and Parameter Effects,” *J. Soil Mechanics and Fnd. Division*, ASCE, Vol. 98, No. SM6, pp. 603-624.

Hushmand, (2016). Seismic Performance of Underground Reservoir Structures. Ph. D. Thesis, Department of Civil, Environmental, and Architectural Engineering, University of Colorado, Boulder.

Hushmand and Associates, Inc. (2016). Geotechnical Centrifuge Modeling of Seismic Response of Underground Reservoir Structures. Data Report prepared for L.A. Dept. of Water and Power.

Hushmand, A., S. Dashti, C. Davis, B. Hushmand, M. Zhang, M. Ghayoomi, J.S. McCartney, Y. Lee, and J. Hu (2016a). “Seismic Performance of Underground Reservoir Structures: Insight from Centrifuge Modeling on the Influence of Structure Stiffness,” *ASCE J.G.G.E.., 10.1061/(ASCE)* GT.1943-5606.0001477, 04016020.

Hushmand, A., S. Dashti, C. Davis, B. Hushmand, Y. Lee, and J. Hu, 2016b, “Seismic Performance of Underground Reservoir Structures: Insight from Centrifuge Modeling on the Influence of Backfill Soil Type and Geometry,” *ASCE JGGE, 10.1061/(ASCE)* GT.1943-5606.0001544, 04016058.

Hushmand, A., S. Dashti, C. A. Davis, J. S. McCartney, and B. Hushmand, 2016, “A Centrifuge Study of the Influence of Site Response, Relative Stiffness, and Kinematic Constraints on the Seismic Performance of Buried Reservoir Structures,” Soil Dynamics and Earthquake Engineering, Elsevier, 88, pp 427-438.Ishibashi, I, and X. Zhang, 1993, “Unified Dynamic Shear Moduli and Damping Ratios of Sand and Clay,” *Soils and Foundations*, Japanese Society of Soil Mech. and Fnd. Engr., Vol. 33, No. 1, pp. 182-191.

Ketcham, S. A., Ko, H. Y., and Sture, S. (1991). ‘‘Performance of an earthquake motion simulator for a small geotechnical centrifuge.’’ *Centrifuge 91*, H.Y. Ko and F.G. McLean, eds., Balkema, Rotterdam, 361–368.

Seed H. B., and I. M. Idriss, 1970, “Soil Moduli and Damping Factors for Dynamic Response Analysis,” Report EERC 70-10, Earthquake Research Center, University of California, Berkeley.

Veletsos, A. S., and A. H. Younan (1994) “Dynamic Modeling and Response of Soil-Wall Systems,” *J. Geo. Engr.*, ASCE, Vol. 120, No. 12, pp. 2155-2179.

Wood, J. H. (1973) “Earthquake-Induced Soil Pressures on Structures,” Report EERL 73-05, Earthquake Engr. Research Laboratory, Caltech.